Topological band structure transitions and goniopolar transport in honeycomb antimonene as a function of buckling

Santosh Kumar Radha [*] and Walter R. L. Lambrecht [†]
Department of Physics, Case Western Reserve University, 10900 Euclid Avenue, Cleveland, Ohio-44106-7079, USA

(Received 24 February 2020; accepted 11 May 2020; published 2 June 2020)

The electronic band topology of monolayer β-Sb (antimonene) is studied from the flat honeycomb to the equilibrium buckled structure using first-principles calculations and analyzed using a tight-binding model and low-energy Hamiltonians. In flat monolayer Sb, the Fermi level occurs near the intersection of two warped Dirac cones, one associated with the p_z orbitals, and one with the $\{p_x, p_y\}$ orbitals. The differently oriented threefold warping of these two cones leads to an unusually shaped nodal line, which leads to anisotropic in-plane transport properties and goniopolarity. A slight buckling opens a gap along the nodal line except at six remaining Dirac points, protected by symmetry. Under increasing buckling, pairs of Dirac points of opposite winding number annihilate at a critical buckling angle. At a second critical angle, the remaining Dirac points disappear when the band structure opens a gap. Spin-orbit coupling and edge states are discussed.

DOI: 10.1103/PhysRevB.101.235111

I. INTRODUCTION

Since the discovery of graphene [1], the world of 2D atomically thin materials keeps expanding. Of special interest are the elemental 2D materials, such as silicene, germanene, and the recently realized and earlier theoretically predicted antimonene and arsenene [2–8]. Unlike their isovalent analog phosphorene (monolayer black phosphorus) [9], which has a more complex buckled structure with fourfold symmetry, monolayer Sb and As are found to prefer the buckled honeycomb structure, known as β-Sb, which is also found in silicene and germanene [10,11]. Interestingly, an almost completely flat honeycomb form was reported to be stabilized epitaxially on a Ag(111) substrate [12]. Thus flat monolayer Sb and As may be the closest analog to graphene but with the interesting difference that there is one additional valence electron which places the Fermi level in between the usual p_z derived Dirac point at K (as in graphene) and a higher lying $\{p_x, p_y\}$ derived Dirac point.

The electronic structure studies thus far report an indirect band gap for equilibrium buckled β-Sb but which undergoes a transition to a semimetallic state under tensile in-plane strain [13,14]. It is related to a transition from a trivial to a nontrivial band gap inversion at Γ. Topological aspects of the band structure of various group-IV and V systems were studied by Huang *et al.* [15] and were also studied in few-layer Sb films as function of thickness [16–18]. Flat honeycomb Sb was shown by Hsu *et al.* [19] to be a topological crystalline insulator. Very recently, Schindler *et al.* [20] determined the topological classification of antimonene as a function of strain from the flat to the buckled form and identified two transitions, which agrees with the present study.

Unlike most of these previous works, we here start from the completely flat honeycomb Sb monolayer and explore systematically how its band structure and topology change as the buckling angle is gradually increased. We will show that the Fermi level position near the intersection of two Dirac cones leads to a number of interesting topological features, from a uniquely shaped nodal line to several new Dirac points which are allowed to move as buckling increases and can mutually annihilate in pairs beyond a critical buckling angle.

Our study is carried out using first-principles density functional theory (DFT) and quasiparticle many-body perturbation theory (MBPT) calculations, with details given in the computational methods. A nearest-neighbor tight-binding model is used to analyze the results and effective low-energy Hamiltonians describing the band features of interest are presented.

Although our predictions here are theoretical, we note that the possibility of stabilizing monolayer Sb in its flat form by epitaxy on Ag(111) has already been demonstrated [12]. In Appendix A, we show using DFT calculations that the flat honeycomb form of monolayer Sb and As is indeed a metastable phase but also show that the band structure features of Sb can still be readily recognized when Sb is placed on top of Ag.

II. COMPUTATIONAL METHODS

The calculations of the structural stability and band structure were performed using density functional theory in the Perdew-Becke-Ernzerhof (PBE) [21] generalized gradient approximation (GGA). Band structures were also calculated using the quasiparticle self-consistent QS*GW* many-body perturbation theory method [22,23]. Here, *GW* stands for the one-electron Green's function and W for the screened Coulomb interaction [24,25]. All calculations were performed using the full-potential linearized muffin-tin orbital (FP-LMTO) method [26,27] using the QUESTAAL package, which is fully

[*]Corresponding author: santosh.kumar@case.edu
[†]walter.lambrecht@case.edu

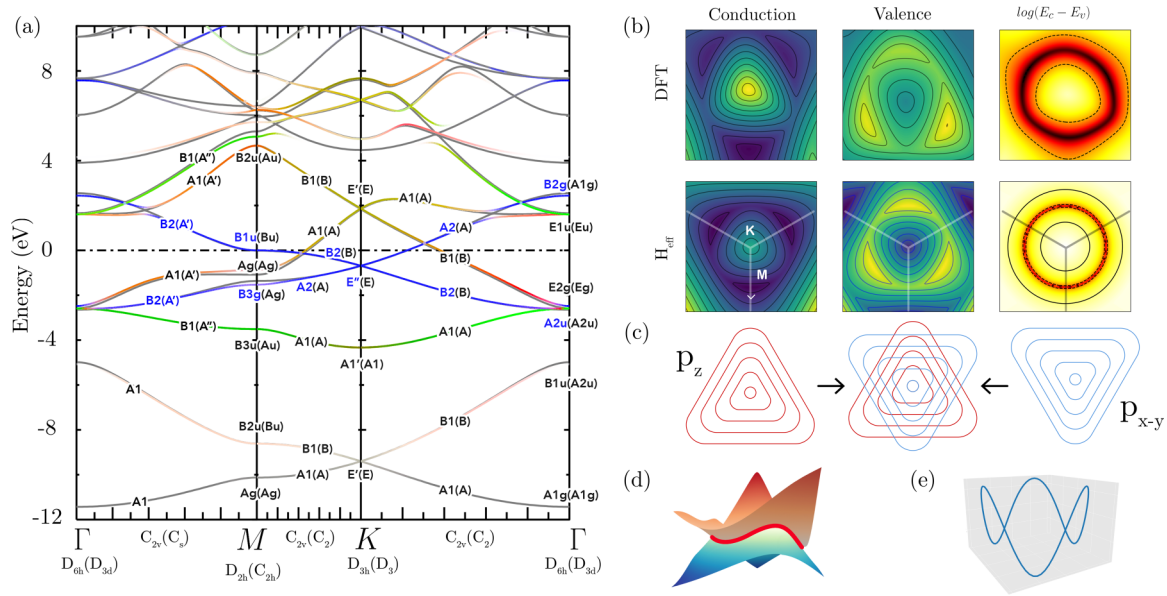

FIG. 1. (a) Symmetry labeled GGA band structure (in eV) of slightly buckled flat monolayer Sb; blue bands indicate bands dominated by p_z, red p_x, green p_y (or their mixture), light grey in bottom two bands s; the bands of completely flat Sb (dark grey) differ only near the points were we see avoided crossings for the buckled case notably between bands 6 and 7 along Γ-K and Γ-M and the slight deviations of bands 4 and 5 near M; (b) Contour plots of two Dirac cones and their intersection (on log scale) in DFT (top) and low-energy effective hamiltonian (bottom); yellow is high, blue is low, explanation in text; (c) schematic of cone intersection (d) 3D view of (DFT) intersecting Dirac cones and (e) nodal line

described in Ref. [28] and available in Ref. [29]. Convergence parameters were chosen as follows: basis set *spdf*-*spd* spherical wave envelope functions plus augmented plane waves with a cutoff of 3 Ry, augmentation cutoff $l_{\max} = 4$, **k**-point mesh, $12 \times 12 \times 2$. The monolayer slabs were separated by a vacuum region of 3 nm. In the *GW* calculations, the self-energy Σ is calculated on a **k** mesh of $5 \times 5 \times 2$ points and interpolated to the above finer mesh and the bands along symmetry lines using the real space representation of the LMTO basis set. The diffusive conductivity tensor σ/τ (apart from the unknown relaxation time) was calculated using the equation

$$\sigma_{\alpha\beta}(E)/\tau = e^2 \sum_n \int \frac{d^3k}{4\pi^3} \delta(E - E_n(\mathbf{k})) v_\alpha v_\beta \qquad (1)$$

with $v_\alpha = \partial E_n(\mathbf{k})/\partial k_\alpha$ The conductivity and Seebeck coefficients are then obtained from

$$\sigma_{\alpha\beta}/\tau = e^2 \int dE \sigma_{\alpha\beta} \left(-\frac{\partial f}{\partial \mu}\right) \approx \sigma_{\alpha\beta}(\mu)$$
$$S_{\alpha\beta} = -\frac{\pi^2 k_B^2 T}{e} \frac{d \ln \sigma_{\alpha\beta}(E)}{dE}\bigg|_{E=\mu} \qquad (2)$$

with $\mu = E_F$ the Fermi energy. The nearest-neighbor tight-binding model used to analyze the results and to obtain the nanoribbon edge states is described in Appendix C.

III. RESULTS

A. Symmetry labeled band structure in (nearly) flat antimonene

We start our discussion with the band structure of flat and slightly buckled monolayer Sb, as shown in Fig. 1(a) and obtained in the generalized gradient approximation (GGA) to DFT. The symmetry labeling of the bands is crucial to our understanding of the protection of the Dirac cones to be discussed. To make this symmetry labeling unambiguous, it is necessary to describe the symmetry operations and character tables in detail, which is done in Appendix B. The pointgroups of **k** applying along each symmetry line in the flat and buckled (labels in parentheses) case are given at the bottom of Fig. 1(a).

Before proceeding with our study of the topological features of interest, we first point out some similarities and differences of the Sb band structure with the well known band structure of graphene. We immediately recognize the Dirac point at K, here labeled E'' corresponding to the p_z-derived bands (shown in blue) with z perpendicular to the layer. In graphene, the Fermi level falls at this point but here, because of the additional valence electron, it lies higher in energy shown as the dash-dotted line and chosen as our reference energy. Another important difference with graphene is that the s orbitals form a separate set of bands at lower energy rather than forming strongly hybridized sp^2 σ bands. This results from a larger $E_p - E_s$ atomic energy difference relative to the hopping interactions between the sites. Nonetheless, we can see a little bit of p contribution in the upper s-band from its slightly reddish color.

The $\{p_x, p_y\}$ derived bands form a separate set of bands (indicated in red (p_x), green (p_y) and their mixture) with another Dirac cone E' at K above the Fermi level. The band structure of $\{p_x, p_y\}$ derived bands on the honeycomb lattice was discussed by Wu and Das Sarma [30] in a tight-binding approximation relevant to optical lattices where only the σ interaction is non zero. Here, both the V_σ and V_π matter. While in a tight-binding model of each set of bands separately, the

energy band derived from s, p_z and $\{p_x, p_y\}$ are symmetric in energy with respect to their atomic energy band center, a feature usually referred to as particle-hole symmetry, the interaction with the higher lying Sb-d bands here breaks this simplification.

The important point is that the Fermi level lies close to the intersection points of the p_z derived and $\{p_x, p_y\}$ derived Dirac cones, one of which lies a little above E_F along Γ-K and the other a little below E_F along Γ-M. We can see that the bands crossing at these points have different symmetry both in the flat and in the slightly buckled case and are thus protected by symmetry. Our symmetry analysis shows that it is a twofold rotation along the Γ-K direction which is maintained both along Γ-K and along K-M even after buckling and protects the existence of these band crossings on the high-symmetry lines. On the other hand, it is the horizontal mirror plane symmetry that protects the nodal line in the flat case.

B. Dirac cones and nodal line

The Dirac cones around K are shown in Figs. 1(b) and 1(c). In the top row of the contour plots, we present the DFT results and below it the corresponding results from an effective low-energy Hamiltonian based on symmetry and a nearest-neighbor tight-binding model, which is described in full detail in Appendix C. In Figs. 1(b)–1(d), by valence (conduction) band we mean bands 5 (6) at each **k**-point numbered in order of increasing energy without regard to band crossings or the nature of the band. Thus, close to K, the conduction band is the empty E' $\{p_x, p_y\}$ derived band, whereas the valence band is the E'' p_z derived band. These respective cones have trigonal symmetry and are seen as the triangular contours in the center of each figure. Beyond the crossing of the cones, the roles of conduction and valence band are reversed. The yellow (high value) regions in the "valence band" are at the intersection of the bands along K-Γ while the dark blue (low value) in the CB correspond to the flat p_z derived band along K-M. We can see that in the center the contours have a triangular shape but are rotated by 30° from each other as is further shown in the schematic sketch (c). This is also shown in a 3D view in part (d) and leads to a nodal line (e) with the Lissajous like shape, where again the blue surface corresponds to the valence band and the brown one to the conduction band. The triangular warping of the energy surfaces results from the terms of order q^2 in an expansion around the point K and can be derived fully analytically from the tight-binding Hamiltonian for the p_z derived bands as is shown in the Appendix C. The linear terms of the Dirac cones are isotropic. Because p_z ($\{p_x, p_y\}$) orbitals are odd (even) with respect to the horizontal mirror plane, they are derived from a separate 2×2 and 4×4 Hamiltonian matrix. Both of these can be further reduced to the eigenvalues of a 1×1 and 2×2 matrix because of the "particle-hole" symmetry within this model and analytical expressions can be derived for them at Γ, K, and near K. The threefold symmetry around K is expected from the pointgroup of K which is D_{3h}. The Dirac cone states can thus be written

$$E_z = \Delta_z \pm v_z q \pm \frac{q^2}{m_z}\cos(3\phi),$$
$$E_{x,y} = \Delta_{x,y} \pm v_{x,y} q \pm \frac{q^2}{m_{x,y}}\cos(3\phi) \tag{3}$$

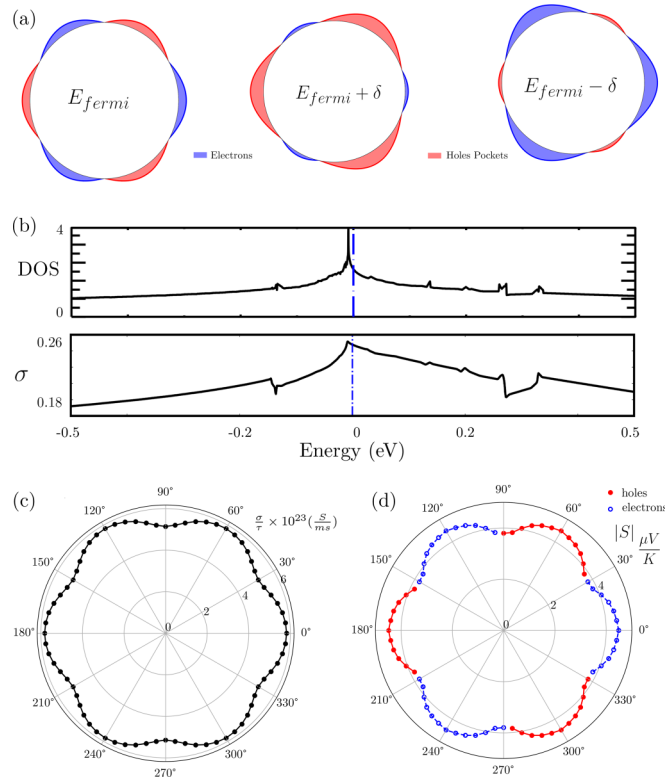

FIG. 2. (a) Fermi surface portions around each point K, (b) DOS and $\sigma(E)/\tau$ (arb. units), (c) angular dependence of diffuse conductivity $\sigma(E_F)/\tau$, and (d) absolute value of thermopower with sign indicated by color (red < 0, blue > 0).

Here, Δ_z and $\Delta_{x,y}$ are the centers of the (E'', E') Dirac cones at K, v_z and $v_{x,y}$ are the Dirac linear dispersion velocities, and m_z and $m_{x,y}$ are effective mass parameters. The actual effective masses depend on the direction of **q** represented by its azimuthal angle ϕ from the x axis (Γ-K direction) leading to a warping of the constant energy lines with threefold symmetry, while the velocity is isotropic. The opposite sign of the mass parameter for the two cones leads to their relative rotation by 30° and is found to be responsible for the interestingly shaped nodal line. Within the tight-binding model (Appendix C) the sign of $m_{x,y}$ is found to be controlled by the ratio of the V_σ and V_π interactions. The situation here is reminiscent of that in AA bilayer graphene but with the difference that here the two Dirac cones have different velocities and warping terms. As a result their intersection is not a simple circular nodal line.

C. Consequences for transport

This unique shape of nodal ring gives rise to an equally interestingly shaped 2D Fermi surface as shown in Fig. 2(a) (obtained from the effective mass Hamiltonian). The Fermi surface can be seen to consist of electron and hole pockets at 60° from each other and exhibits electron hole contact points (EHCP) where discontinuities occur in the band velocity. This figure shows that the carrier type changes from electron to hole type every 60° as we go around the Fermi surface, an effect that has been named goniopolarity [31]. Furthermore, depending on the precise location of the Fermi energy, which could in principle be varied by doping or gating, the electron

or hole transport could be larger or smaller as the direction is changed in-plane. This situation is somewhat similar to the case of a tilted nodal line in a 3D **k** space, where interesting effects on the frequency dependent conductivity result from the cyclide geometry of the resulting Fermi surface [32].

Here, we have calculated the static diffuse longitudinal conductivity $\sigma(E_F,\phi)/\tau$ apart from the, at this point unknown, relaxation time τ as function of azimuthal angle ϕ and the thermopower (or Seebeck coefficient) which is proportional to $d\ln\sigma(E,\phi)/dE|_{E=E_F}$ and whose sign reflects the charge of the carriers. These are shown in Figs. 2(c) and 2(d) and show that the conductivity has modest anisotropy at the ∼14% level but the thermopower changes discontinuously from positive to negative at the EHCPs. Interestingly, it is positive for the directions corresponding to electron transport because $d\sigma/dE|_{E_F} < 0$. This is because the conductivity varies rapidly with energy near E_F and the Fermi energy occurs just above a peak in the $\sigma(E,\phi)$ related to a logarithmic singularity in the density of states (DOS) resulting [see Fig. 2(b)] from the saddle-point band structure at the point B_{1u} at M. Inserting an order of magnitude estimate of $\tau = 10^{-13}$s would give a resistivity of order 0.2 $\mu\Omega$ cm and a thermopower of order 5 μV/K, which is relatively high due to the Fermi level's occurrence near a peak in the DOS. The unique feature here however is the discontinuous angular dependence of the thermopower. Numerous other opportunities in the optical conductivity and magnetotransport related to this unique 2D nodal line remain to be explored. While we pointed out the goniopolarity here for the completely flat system which hosts a nodal line, this property is expected to hold up even after somewhat buckling the system, so for less strong in-plane tensile strains, as long as some thermal excitation or doping provides carriers in the corresponding slightly gapped bands.

D. Changes in topology due to buckling

Next, we address the changes in band structure due to buckling. The buckling leads to an interaction between the p_z and $\{p_x, p_y\}$ derived energy bands because the horizontal mirror plane symmetry no longer applies. We assume here that the bond-lengths between Sb atoms stays the same but the in-plane lattice constant shrinks as the buckling is increased. This is qualitatively consistent with the relaxation results [15] showing a decrease in vertical distance between the Sb atoms d as function of in-plane lattice constant a. Thus in our tight-binding model the V_σ and V_π interactions stay the same but their relative contribution to the hopping integrals changes. Within the tight-binding model (Appendix C) the interaction terms between p_z on the one hand and $\{p_x, p_y\}$ on the other hand are proportional to $(V_\sigma - V_\pi)$ and to $\sin(2\theta)$ where θ is the buckling angle. For small buckling, the coupling is thus linear in θ. The symmetry labeled band structure shows that in the six high-symmetry directions around K the crossing is protected by symmetry and thus the interaction needs to go to zero every 60°. Hence by symmetry, the low-energy Hamiltonian describing the behavior near these Dirac cones can be written

$$H^{\text{buckled}}_{\mathbf{K}+\mathbf{q}} = \begin{bmatrix} \Delta_{x,y} + \frac{q^2\cos(3\phi)}{m_\pi} - qv_{x,y} & A\theta\sin(3\phi) \\ A\theta\sin(3\phi) & \Delta_z + \frac{q^2\cos(3\phi)}{m_z} + qv_z \end{bmatrix} \tag{4}$$

with A some constant and a $\sin(3\phi)$ behavior of the off-diagonal coupling. Figure 3 shows the effect of buckling on the nodal line around K by plotting the difference between conduction and valence band in a logariphmic plot and verifies the existence of six Dirac points.

Increasing the buckling either in the DFT or in the tight-binding model, we find that the Dirac touching points around K move closer toward M along the K-M-K' line and closer to Γ along the K-Γ line. At some critical angle, the two Dirac points along K-K' annihilate each other when they reach M. This is shown in Fig. 3(b) In the DFT results, this occurs for about $\theta_c \approx 7°$.

The reason why they can annihilate is that they have opposite winding number +1 and −1. The winding number was calculated either from the effective low-energy Hamiltonian or by calculating the Berry curvature in the tight-binding model (see Appendix D) The winding number, which can be thought of as a topological charge, is a conserved quantity [33]. Thus the only possible way to remove Dirac cones is to merge and annihilate them. The reason for the merging of the Dirac cones is related to time reversal symmetry, which guarantees that there is an equivalent and oppositely charged Dirac cone at $-\mathbf{k}$ for every Dirac cone at **k**. Thus by symmetry, these Dirac cones of opposite sign come together and annihilate at the two types of time reversal invariant points Γ and M.

Montambaux *et al.* [34] have analyzed the merging of 2D Dirac points in terms of a universal Hamiltonian, which shows that near such a point the bands correspond to a massive dispersion in one of the in-plane directions and a massless one in the orthogonal in-plane direction, which leads to an unusual $\sqrt{E}$ onset of the density of states [35], which leads also to interesting changes in Landau levels [36]. The behavior of the energy surfaces near the merging is shown in Fig. 3(d).

After the merging of the Dirac points at M, upon further buckling, the Dirac points along K-Γ keep moving closer to Γ. When they reach Γ at a second critical angle of about 27°, they annihilate in pairs and the gap at Γ beyond this buckling first closes and then reopens, indicating a band inversion between bands of different symmetry label. The evolution of the bands in the tight-binding model is shown in more detail in Appendix C. The E' and E'' points splitting increases significantly with increasing buckling. With increasing buckling the distinction between p_z and $\{p_x, p_y\}$ becomes less and less meaningful and a new type of hybridization between all three bands forming a bonding set of bands and antibonding set of bands emerges for the fully buckled ground state of the system. The opening of the gap corresponds to the transition from a topologically nontrivial to a trivial gap at Γ, which was studied earlier in literature [15] starting from the equilibrium large buckling by reducing the buckling under a tensile in-plane strain. We should clarify here that by nontrivial we mean in the sense of a topoligical insulator (TI) protected by time reversal. The system even in its fully buckled form has nontrivial topoligal crystal insulator (TCI) character [37].

E. Spin-orbit coupling effects

Turning on spin orbit coupling (SOC), a gap opens up at each of the Dirac points. We can see that it is larger for the

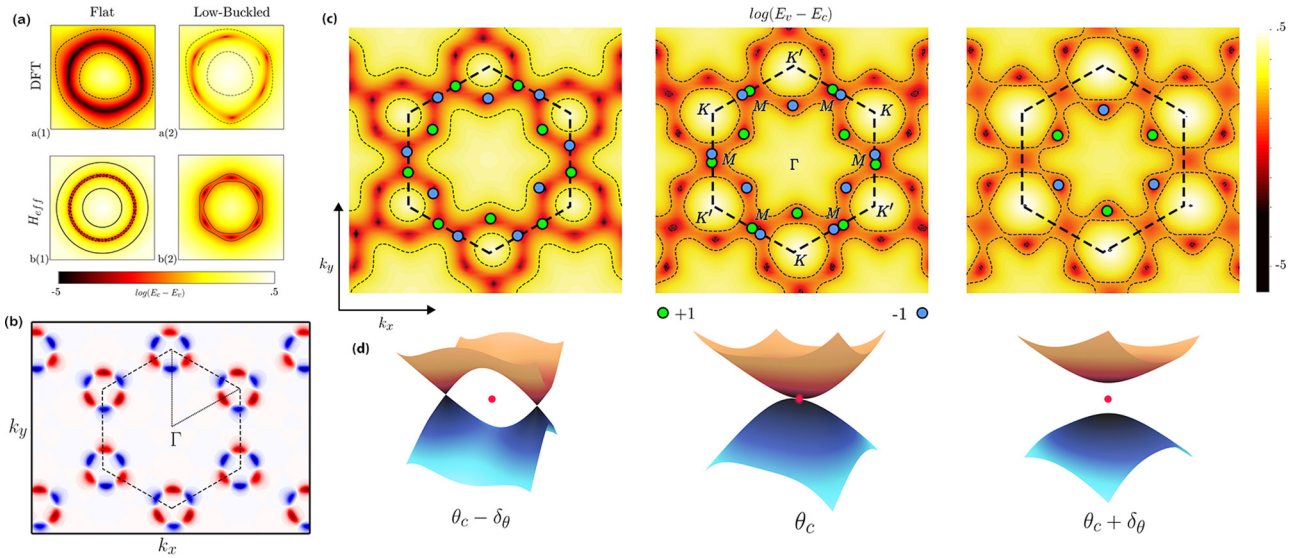

FIG. 3. (a) Nodal line gap opening and formation of six Dirac points in slightly buckled honeycomb, (b) Berry flux around each of the Dirac cones surrounding each K point, (c) movement and merging of Dirac cones as buckling angle increases, and (d) corresponding behavior of constant energy surfaces around M (red dot).

upper E' point (0.56 eV) than at the lower E'' point (0.17 eV) and intermediate at the Dirac points near E_F. The nontrivial nature of the band crossings leads to topologically required edge states when the gap is opened by SOC. For the nearly flat case, these were studied in Ref. [19]. However, we need to keep in mind how the gaps at the K-M and Γ-K Dirac points are placed energetically relative to each other. While up to this point, we considered mostly generic properties which are topologically invariant, we now need to worry about the accuracy of the band structure and in particular the correct slope and placement of the different Dirac points relative to each other. To this end, we perform the band structures in the QSGW approach which is known to give much more accurate single particle excitations than DFT in a semilocal approximation. We can see that this affects the band velocities of the Dirac cones and the energy difference of the E', E'' Dirac points at K. For the fully buckled equilibrium system QSGW gives a gap of 2.9 eV, significantly larger than the 1.3 eV obtained in GGA and somewhat larger than the 2.28 eV from hybrid functional calculations [38]. In Fig. 4, we can see that the highest VBM at the Dirac point along Γ-K lies at the same energy as the lowest conduction band at the Dirac point along K-M. So, the system is an indirect zero gap semiconductor. Because the SOC is weaker in arsenene, there is then a nonzero indirect overlap between the occupied and empty bands at different Dirac points (see Appendix E). The unique feature of this band structure is that it should have a topologically spin polarized edge state associated with these SOC induced spin-texture inverted gaps at specific **k** points, even though the overall gap of the system is zero or slightly negative. Such a situation has been labeled a gapless topological insulator (GTI). It has been proposed to possibly occur due to electron-electron interaction effects [39] but is here found even in the independent particle approximation.

F. Topological edge states

As is well known, topological features in the band structure are closely related to protected edge states. The tight-binding model allows us to study the formation of these edge states explicitly in a finite nanoribbon. We choose to cut the honeycomb lattice along the zigzag direction and keep it periodic in the direction perpendicular to it but with a width of 60 unit cells. As further confirmation, Fig. 5(b) shows a smaller 6 unit cell nanoribbon, calculated at the DFT level with the resulting

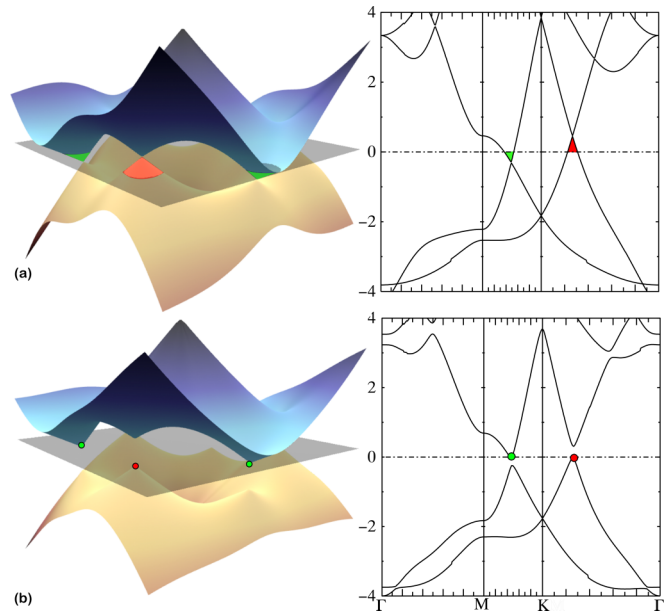

FIG. 4. QSGW band dispersion for the low-buckled system without (top) and with (bottom) SOC and the corresponding conical energy surfaces. Energies in eV.

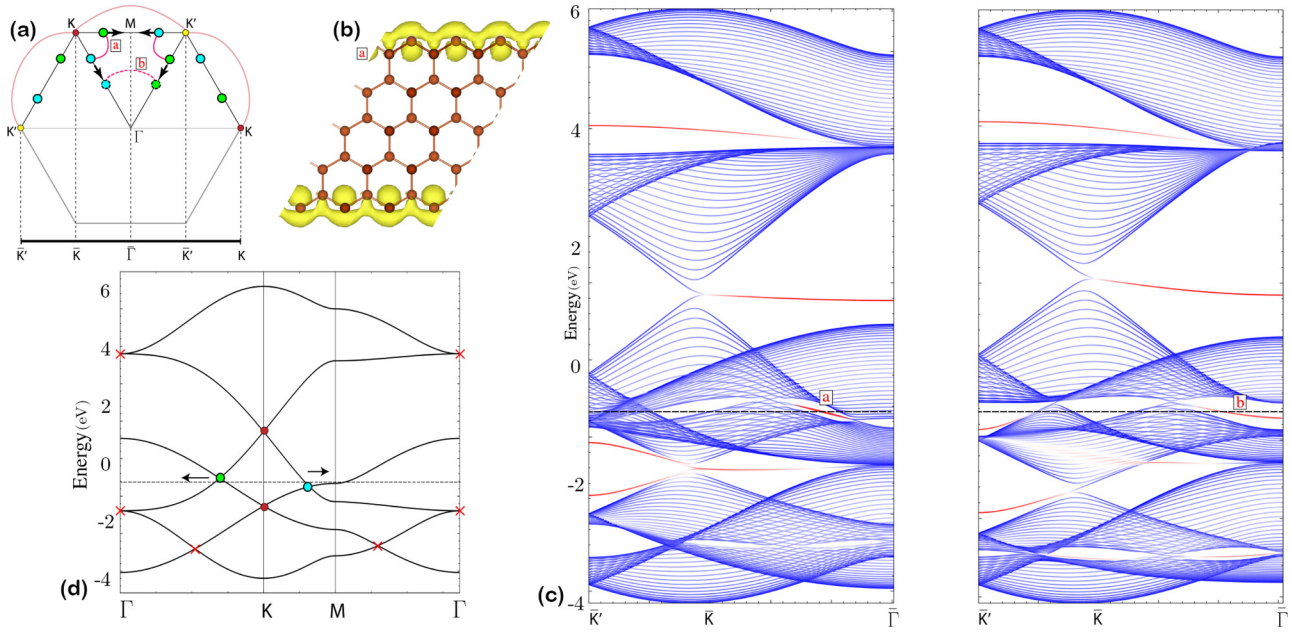

FIG. 5. (a) Folding of 2D Brillouin zone onto 1D Brillouin zone in nanoribbon indicating schematically the Dirac points linked by edge states and their motion under increased buckling; (b) six unit cell side nanoribbon with surface state from DFT; (c) band structure of nanoribbon in tight-binding model indicating the topologically protected edge states (in red) associated with Dirac point pairs labeled as in (a) for two buckling angles, one before and one after the merging of Dirac cones at M; and (d) 2D tight-binding band structure for the low buckling case.

edge state. The Brillouin zone folding is shown in Fig. 5(a). The Dirac points are color coded according to their winding number and linked by lines for the pairs that will be connected by corresponding edge states. These connections found here explicitly from the numerical calculations are consistent with the theoretical considerations of Ryu and Hatsugai [40] and with explicit calculation of the Zak phase along different sections of $\mathbf{k}_\parallel$ showing that the edge states occur in the region where the Zak phase is π and hence nontrivial. Note that this depends not only on the type of edge but also on the symmetry type of orbital involved in these bands. For instance, the edge states emanating from the p_z derived Dirac cone at K at about -2 eV extends between $\bar{K}$ and $\bar{K}'$ as is the case in graphene. However, the edge state in the gap near the Fermi level, marked (b) in the right panel of Fig. 5(c), connects the Dirac point with $\bar{\Gamma}$ and continues in the next Brillouin zone back to the periodically repeated Dirac point. This difference from graphene results from the different type of orbitals involved and the region where the Zak-phase is nontrivial.

The main part of the figure shows the 1D band structures indicating the edge states in red labeled to identify them with particular Dirac point pairings in the Brillouin zone figure following the same labeling. We here focus mainly on the Dirac cones near the Fermi level but other ones can be seen at energies farther away from the Fermi level. These are related to other linear band crossings and the Γ-point degenerate levels (marked by $\times$) which can be seen to occur in the tight-binding band structure for the 2D periodic band structure at energies farther removed from the Fermi surface. In the low-buckling case, from top to bottom, the edge states are related to the E_{1u} state at Γ, the E' state, the connection between Γ-K and K-M Dirac points, the E'' Dirac point and the E_{2g} state at Γ, with the latter two interacting along $\bar{K}$-$\bar{K}'$. Finally, an edge state connected to the lowest energy Dirac crossings along Γ-K can be seen along $\bar{K}$-$\bar{\Gamma}$. The edge states associated with the low-energy crossing along Γ-M cannot be seen in this nanoribbon because the Γ-M direction is the one along which we fold the bands. Because various of these edge states connect Dirac points not along a high-symmetry direction, one expects them to be present for other cut-outs of the 2D lattice in arbitrary directions.

IV. CONCLUSIONS

In summary, in this paper we have shown that monolayer Sb and As in the honeycomb structure exhibit a rich behavior in terms of topological features. The system evolves from a unique type of nodal line in the flat case to a series of six symmetry protected Dirac points surrounding each K point which move and annihilate first in pairs of opposite winding number at a first critical buckling angle and subsequently undergo a second topological transition when a trivial gap opens at Γ. These result from the changing contribution of σ and π interactions between the orbitals as function of buckling. The nodal line is here predicted to lead to a highly anisotropic in-plane Seebeck coefficient reflecting goniopolarity. A multitude of edge states are predicted as well as a gapless topological insulator behavior when spin-orbit coupling is included which results from the energy straddling of the small gaps opening at the symmetry protected Dirac states in the system.

Finally, the reader may ask himself if this is a purely theoretical exercise. As mentioned, while the equilibrium structure of monolayer Sb is buckled and already in the region where the gap is fully opened. Nonetheless the flat form can be stabilized by tensile in-plane strain, as for example occurs in an epitaxial situation on Ag [12]. We realize that it is not trivial at all to gradually change this epitaxial strain in

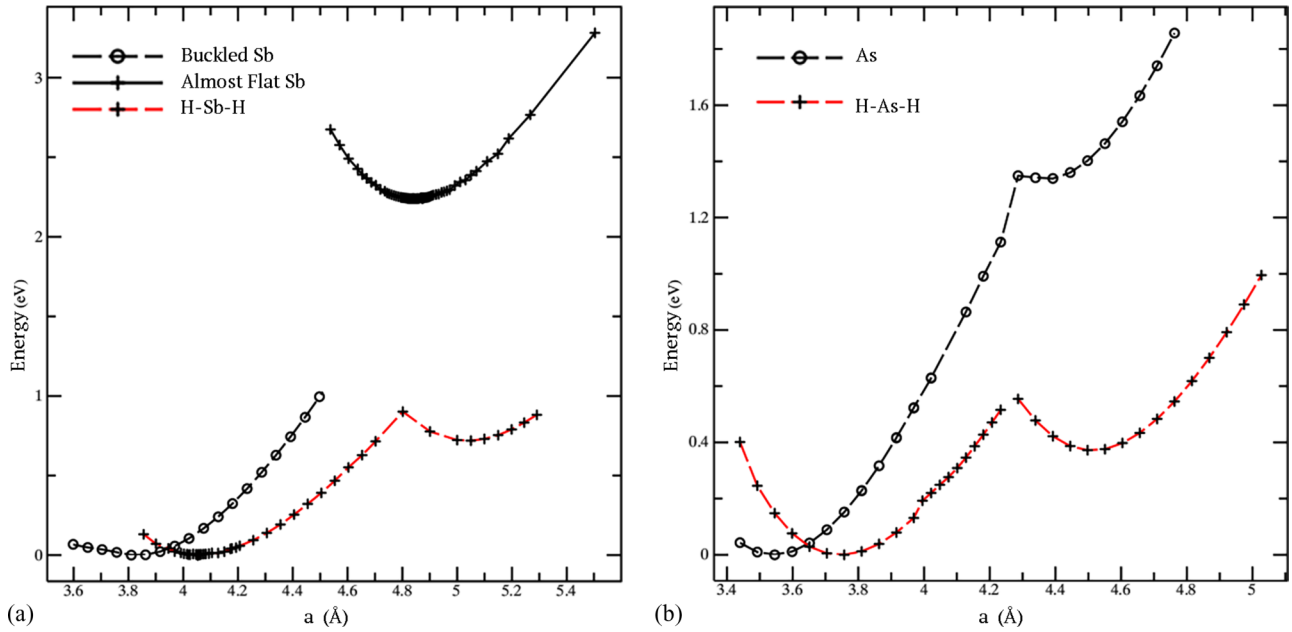

FIG. 6. Fully relaxed total energy per two-atom unit cell as function of in-plane lattice constants for Sb (left) and As (right).

experiment. However, it is not entirely inconceivable that one could construct suspended monolayer Sb membranes in which the tensile strain could be controlled by nano mechanical means. One could for example bend the substrate to increase the strain. Or one may at least envision to control different amounts of in-plane strain in different samples by chemically modifying the underlying substrate and thus achieve different strain states in each of the regimes we describe in our paper.

ACKNOWLEDGMENTS

This work was supported by the US Department of Energy-Basic Energy Sciences under Grant No. DE-SC0008933. The calculations made use of the High Performance Computing Resource in the Core Facility for Advanced Research Computing at Case Western Reserve University.

APPENDIX A: STABILITY AND METASTABILITY OF FLAT AND BUCKLED 2D MONOLAYERS

Here we discuss the stability of flat *vs.* buckled forms of 2D monolayer Sb and As in the β structure. In Fig. 6, we show the results of first-principles density functional calculations using the PBE-GGA functional for the total energy as function of in-plane lattice constant of the honeycomb lattice. In the buckled case, the structure for a given a is allowed to fully relax, leading to a relative high buckling angle of $\sim 33^\circ$ defined by $\tan\theta = \sqrt{3}d/a$ with d the vertical distance between Sb atoms along the z axis and a the in plane lattice constant. We can see that a nearly flat structure, with higher in-plane lattice constant, exists as a second metastable minimum.

The dynamical stability of monolayer honeycomb Sb was studied by Zhao *et al.* [18] by means of phonon calculations in the harmonic approximation. It shows that up to a 19% in-plane tensile strain, the system is dynamically stable while beyond this critical strain, imaginary phonon modes appear around K and near Γ. We have confirmed these results using the QUANTUM ESPRESSO code [41] and also found that the flat form shows imaginary modes. However, at finite temperature anharmonic terms in the potential could still keep the system from becoming unstable. Typically a dynamic symmetry breaking instability of this type only occurs below a critical temperature because, at higher displacement, fourth order terms become dominant. Secondly, what one needs to consider here is not the stability of the free-standing flat form of Sb but the flat form under an applied tensile in-plane strain. This would actually require one to check the positive definiteness of $\partial\mathcal{H}/\partial u_i \partial u_j$ where $\mathcal{H} = \mathcal{U} - V\eta\cdot\sigma$ with $\mathcal{U}$, the internal energy, η the strain and σ the stress and V the volume, as function of atomic displacements in the cell u_i. Such anahrmonic calculations and including the strain explicitly in the formulation are not at all trivial [42]. Fortunately, they are not needed because the experiment has already confirmed the stability of the material in flat form [12].

Finally hydrogenating the structure with H on top or below the Sb on alternating Sb, is seen to lower the energy of the flat Sb structure significantly although it still has higher energy than the equilibrium structure. Similar results are found for As. In the this paper, we have not studied the hydrogenated form. In that case the Fermi level lies at the $\{p_x, p_y\}$-derived E' Dirac point at K. This case was studied in Refs. [43,44]

Although free standing monolayer Sb in the β structure clearly has a high buckling angle, it has unambiguously been demonstrated experimentally that the flat or nearly flat structure can be stabilized by epitaxial in-plane tensile strain by putting the Sb on a Ag(111) structure [12]. The band structure of free standing flat monolayer Sb is discussed in the main paper. For comparison, we here show the band structure of a ten-layer-thick Ag layer with a monolayer of Sb on

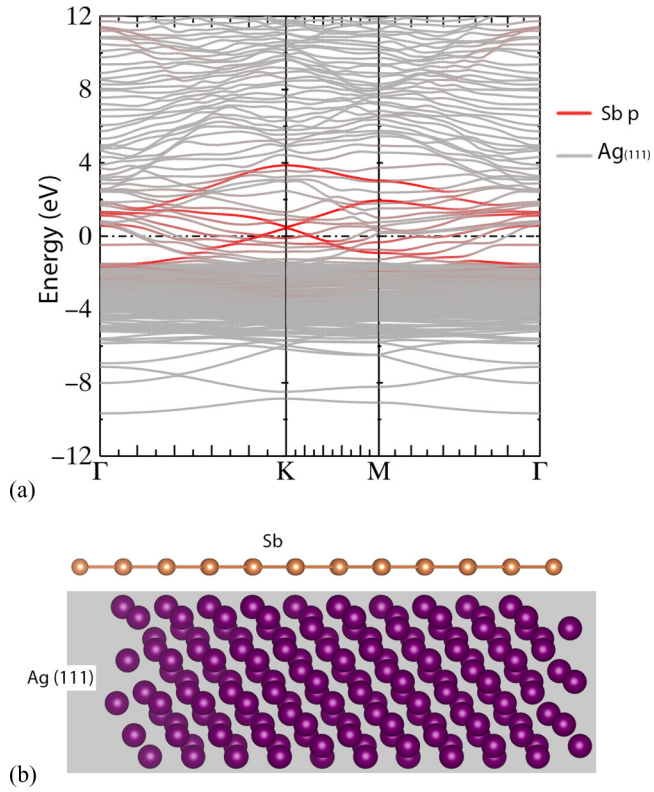

FIG. 7. Band structure of a Ag (111) slab with Sb monolayer adsorbed.

top in Fig. 7. The structure was relaxed with DFT before calculating the band structure. The bands weighted by their Sb contribution are shown in red. This shows that the features of monolayer Sb can still be recognized clearly on top of the Ag background, especially in the important region near the Dirac crossings and Fermi energy where the Ag density of states is low. This confirms the x-ray photemission (XPS) investigations by Shao *et al.* [12] indicating a weak interaction between substrate and monolayer, which could maintain at least approximately its relevant properties while providing the required in-plane tensile strain to stabilize the flat form.

This shows that there is a route forward to experimentally investigate the band structure aspects studied in the main paper by means of epitaxial stabilization and the investigation of monolayer Sb under high tensile strain in a flat or nearly flat form is not just a theoretical exercise but could potentially be realized experimentally by adjusting the coupling to the underlying substrate or varying the lattice constant of the substrate. Of course, for topologically induced effects on the transport, one would then also have to consider scattering to and from the underlying Ag band structure and the effects of the substrate symmetry breaking. Nanoscale mechanical systems can potentially also be designed for free standing membranes suspended over a hole in the substrate as is currently done for graphene, black phosphorous etc. What level of strain can be sustained in such systems is not yet clear but 2D systems are known to be able to sustain larger strains than 3D systems. Alternative substrates, like h-BN with van der Waals type interactions might also be considered as a way to maintain the required tensile strain while at the same time minimizing the interactions so as to preserve the properties of flat monolayer Sb [19]. In any case, the properties studied here for free-standing flat monolayer Sb should serve as a well-defined theoretical limit of the physically realizable flat Sb on a suitable substrate with sufficiently weak interactions. The perturbations caused by such interactions would have to be considered in future work.

APPENDIX B: SYMMETRY ANALYSIS

Here we present the details of the symmetry labeling of the band structure. Flat monolayer Sb in the honeycomb structure has the same space group and point group as graphene. Several prior papers have addressed the symmetry labeling of the bands in graphene [45–47] but still some confusion exists because of the nonuniqueness in specifying the symmetry operations and irreducible representations. The point group of the crystal is D_{6h} and this is also the point group at Γ. The character table is given in Table I. Note that in D_{6h} there are

TABLE I. Character table of D_{6h}.

D_{6h}		E	C_2	$2C_3$	$2C_6$	$3U_2$	$3U_2'$	i	σ_h	$2S_6$	$2S_3$	$3\sigma_v$	$3\sigma_v'$
Γ_1^+	A_{1g}	1	1	1	1	1	1	1	1	1	1	1	1
Γ_2^+	A_{2g}	1	1	1	1	−1	−1	1	1	1	1	−1	−1
Γ_4^+	B_{1g}	1	−1	1	−1	1	−1	1	−1	1	−1	1	−1
Γ_3^+	B_{2g}	1	−1	1	−1	−1	1	1	−1	1	−1	−1	1
Γ_6^+	E_{2g}	2	2	−1	1	0	0	2	2	−1	1	0	0
Γ_5^+	E_{1g}	2	−2	−1	1	0	0	2	−2	−1	1	0	0
Γ_1^-	A_{1u}	1	1	1	1	1	1	−1	−1	−1	−1	−1	−1
Γ_2^-	A_{2u}	1	1	1	1	−1	−1	−1	−1	−1	−1	1	1
Γ_4^-	B_{1u}	1	−1	1	−1	1	−1	−1	1	−1	1	−1	1
Γ_3^-	B_{2u}	1	−1	1	−1	−1	1	−1	1	−1	1	1	−1
Γ_6^-	E_{2u}	2	2	−1	1	0	0	−2	−2	1	−1	0	0
Γ_5^-	E_{1u}	2	−2	−1	1	0	0	−2	2	1	−1	0	0

TABLE II. Character table of D_{3h}.

D_{3h}		E	$2C_3$	$3U_2'$	σ_h	$2S_3$	$3\sigma_v$
K_1	A_1'	1	1	1	1	1	1
K_2	A_2'	1	1	−1	1	1	−1
K_6	E'	2	−1	0	2	−1	0
K_3	A_1''	1	1	1	−1	−1	−1
K_4	A_2''	1	1	−1	−1	−1	1
K_5	E''	2	−1	0	−2	1	0

two sets of twofold rotations lying in the plane. We choose U_2 to pass through the atoms, while the U_2' pass through the bond centers. In reciprocal space, this implies that U_2 lies along the Γ-M lines and U_2' lies along the Γ-K lines. The corresponding mirror planes $i * U_2 = \sigma_v$ and $i * U_2' = \sigma_v'$ are perpendicular to these axes, so σ_v goes through the bond centers and σ_v' goes through the atoms. We choose the lattice vectors as $\mathbf{a}_1 = a\hat{\mathbf{x}}$, $\mathbf{a}_2 = -\frac{1}{2}a\hat{\mathbf{x}} + \frac{\sqrt{3}}{2}a\hat{\mathbf{y}}$ and one of the points K in the Brillouin zone thus lies along x and one of the points M lies along y. The K points rotated by 60° we label K'. We note points K rotated by 120° are equivalent in that they are related by a reciprocal lattice vector whereas K and K' are not. Likewise we denote the M points rotated by 60°, M' and rotated by 120° as M''. These are nonequivalent but rotating them by 180° gives equivalent M points.

The group D_{6h} can be viewed as the direct product $D_6 \otimes C_i$ where C_i is the group consisting of the identity and the inversion. (It could also be viewed as $C_{6v} \otimes C_i$ or $C_{6v} \otimes C_s$ or $D_6 \otimes C_s$ with C_s the group formed by $\{E, \sigma_h\}$ and this is the reason behind some of the discrepancies between previous symmetry labelings.) The irreducible representations follow the usual notation in which subscript g means even with respect to inversion and u means odd with respect to inversion. The corresponding labels of the Koster notation [48] are also included. Although the symmetry aspects for graphene and Sb are the same, a difference is that the s-p splitting is larger in Sb relative to the hopping interactions and hence the s states form separate bands from the atomic p-state derived bands. The s states are even in the horizontal mirror plane and form bonding an antibonding combinations on atoms A and B in the unit cell: $(s_A + s_B)/\sqrt{2}$ and $(s_A - s_B)/\sqrt{2}$. The operations C_2, C_6, U_2', i, S_6, σ_v change sublattices A to B and vice versa. Thus it is clear that the bonding state belongs to A_{1g} and the antibonding state to B_{1u}. The p_z states are odd *vs.* the σ_h and are thus decoupled by symmetry from the s and p_x, p_y. Again they form bonding and antibonding states $(p_{zA} + p_{zB})/\sqrt{2}$ and $(p_{zA} - p_{zB})/\sqrt{2}$ which are now respectively of symmetry A_{2u} and B_{2g}. The p_x and p_y build the representations E_{2g} and E_{1u}.

Now, the group of $\mathbf{k}$, $\mathcal{G}_\mathbf{k}$, consists of those operations that turn $\mathbf{k}$ into itself up to a reciprocal lattice vector. For point K, which we choose along the x-axis, these are $\{E, 2C_3, 3U_2', \sigma_h, 2S_3, 3\sigma_v\}$, which build the group D_{3h}. At M, the group $\mathcal{G}_{\mathbf{k}_M}$ consists of $\{E, C_2, U_2, U_2', i, \sigma_h, \sigma_v, \sigma_v'\}$ building the group D_{2h}. The character tables of these groups are given in Tables II and III. Note that in the group D_{3h} representations labeled by superscript $'$ are even with respect to the σ_h and $''$ are odd. In D_{2h} note that which irrep is called

TABLE III. Character table of D_{2h}.

D_{2h}		E	$C2$	$U_{2(y)}$	$U_{2(x)}'$	i	σ_h	$\sigma_{v(xz)}$	$\sigma_{v(yz)}'$
M_1^+	A_g	1	1	1	1	1	1	1	1
M_3^+	B_{1g}	1	1	−1	−1	1	1	−1	−1
M_2^+	B_{2g}	1	−1	1	−1	1	−1	1	−1
M_4^+	B_{3g}	1	−1	−1	1	1	−1	−1	1
M_1^-	A_u	1	1	1	1	−1	−1	−1	−1
M_3^-	B_{1u}	1	1	−1	−1	−1	−1	1	1
M_2^-	B_{2u}	1	−1	1	−1	−1	1	−1	1
M_4^-	B_{3u}	1	−1	−1	1	−1	1	1	−1

B_{2g} or B_{3g} depends on the choice of U_2 or U_2' being chosen as first or second set of twofold axes in the xy plane. We added another label to indicate specifically which axes are chosen for the M lying along y.

Along the Γ-$K = T$ axis the symmetry operations remaining are $\{E, U_{2(x)}', \sigma_h, \sigma_{v(xz)}\}$ building the group C_{2v}. The irreps of this group depend on which of the mirror planes one chooses as first. We here choose σ_h as first mirror plane. Along Γ-$M = \Sigma$, the group is also C_{2v} but now the symmetry elements remaining are $\{E, U_{2(y)}, \sigma_h, \sigma_{v(yz)}'\}$. Finally along the line M-K the group is the same as along Γ-K. The character tables used are given in Table IV.

Next, we consider the modifications that occur upon buckling. In this case, the mirror planes through the atoms remain but the twofold rotation through the atoms is no longer valid. Similarly, the rotation axis through the bond center remains but the mirror plane through the bond axis is no longer valid. The sixfold rotations also are no longer valid but the inversion remains. The corresponding changes from flat to buckled in the groups $\mathcal{G}_\mathbf{k}$ are given in Table V. The resulting group is D_{3d} and its character table is given in Table VI.

We can thus easily convert the labels from the D_{6h} case to the D_{3d} case according to Table VII. The same holds for the odd versus inversion irreps labeled by the u subscript.

Now at K, the group becomes D_3 because we loose the inversion. The character table thus consist just of the upper left block in Table VI. The irreps stay the same as at Γ but without the g, u subscripts. At M we now have the group C_{2h} consisting of $\{E, U_{2(x)}', i, \sigma_{v(yz)}'\}$. Its character table is given in Table VIII.

Along the line Γ-K the group is C_2 consisting of $\{E, U_{2(x)}'\}$. The same applies to the line M-K. The character table is

TABLE IV. Character table of C_{2v}.

C_{2v}	$\Gamma - K$ $\Gamma - M$	E E	$U_{2(x)}'$ $U_{2(y)}$	σ_h σ_h	$\sigma_{v(xz)}$ $\sigma_{v(yz)}'$
$(T, \Sigma)_1$	A_1	1	1	1	1
$(T, \Sigma)_3$	A_2	1	1	−1	−1
$(T, \Sigma)_2$	B_1	1	−1	1	−1
$(T, \Sigma)_4$	B_2	1	−1	−1	1

TABLE V. Groups $\mathcal{G}_{\mathbf{k}}$ for flat and buckled cases.

	Γ	Γ-M	M	M-K	K	K-Γ
Flat	D_{6h}	C_{2v}	D_{2h}	C_{2v}	D_{3h}	C_{2v}
		$\{E, U_{2(y)}, \sigma_h, \sigma'_{v(yz)}\}$		$\{E, U'_{2(x)}, \sigma_h, \sigma_{v(xz)}\}$		$\{E, U'_{2(x)}, \sigma_h, \sigma_{v(xz)}\}$
Buckled	D_{3d}	C_s	C_{2h}	C_2	D_3	C_2
		$\{E, \sigma'_{v(yz)}\}$		$\{E, U'_{2(x)}\}$		$\{E, U'_{2(x)}\}$

given in Table IX. Along Γ-M, the group is C_s consisting of $\{E, \sigma'_{v(yz)}\}$ with characters given in Table X.

We may also consider a flat structure but making the A and B atoms different. This would apply to the case of monolayer h-BN. Then starting from D_{6h} we loose the inversion but we keep the horizontal mirror plane. The group at Γ in that case is D_{3h} consisting of $\{E, 2C_3, 3U_2, \sigma_h, 2S_3, 3\sigma'_v\}$. The group at K in that case is the group C_{3h} consisting of $\{E, 2C_3, \sigma_h, 2S_3\}$. At M, the group becomes C_{2v} consisting of $\{E, U_2, \sigma_h, \sigma'_v\}$. Along the lines Γ-K and M-K the group is C_s consisting of $\{E, \sigma_h\}$ and along Γ-M it is the same as at M.

Finally, making the system both buckled and breaking the inversion. Then the group at Γ is only D_3, containing $\{E, 2C_3, 3U_2\}$. At K, it becomes C_3 at M and along Γ-M it becomes C_2 with only elements $\{E, U_2\}$ along Γ-K and M-K there is no symmetry left at all.

The character table of C_3 is given in Table XI. We note that in the group C_3, Koster *et al.* [48] labels the two irreps which cannot be made real as two separate irreps while in the 'chemical' notation, they are both labeled E. This is because if one ignores spin these two irreps are each other's complex conjugate and become degenerate by time reversal. They form a Kramers doublet. However, taking into account the spin 1/2 no degeneracy between the two occurs because time reversal takes spin up into spin down. Adding the horizontal mirror plane just adds another label $'$ or $''$ for even or odd under that operation. Thus we can see that that the degenerate levels E in the buckled case or E' and E'' would be allowed to split and open a gap. This is well known to open the gap in the honeycomb BN case.

APPENDIX C: TIGHT-BINDING MODEL

In this section, we construct a nearestins-neighbor tight-binding Hamiltonian for the Sb-p derived orbitals. The structure is shown in Fig. 8. For the bands near the Fermi level, one can ignore the contribution of s states as they occur at much lower energy as seen in the previous section. Separating the orbitals according to their sublattice A, B, the Hamiltonian takes the block form:

$$H = \begin{array}{c} \\ A \\ B \end{array} \begin{array}{c} \begin{array}{cc} A & B \end{array} \\ \begin{pmatrix} \bar{\Delta} + \mu_A I_{3\times 3} & \bar{H} \\ \bar{H}^* & \bar{\Delta} + \mu_B I_{3\times 3} \end{pmatrix} \end{array}. \tag{C1}$$

Here,

$$\bar{\Delta} = \begin{bmatrix} \Delta_{x,y} & & \\ & \Delta_{x,y} & \\ & & \Delta_z \end{bmatrix} \tag{C2}$$

gives the energy shift of the atomic p orbitals from the zero reference energy. We included here the fact that the on-site diagonal energy for p_z orbitals may be different from that of $\{p_x, p_y\}$ orbitals. We can also switch on a different potential (μ_A, μ_B) on each sublattice and examine which band crossings open up as a gap in response. The off-diagonal AB blocks involve the Bloch sum over the three nearest neighbors:

$$\begin{aligned} \bar{H} = {} & T_1(V_\pi, V_\sigma, \theta) e^{i\mathbf{k}\cdot\boldsymbol{\delta}_1} + T_2(V_\pi, V_\sigma, \theta) e^{i\mathbf{k}\cdot\boldsymbol{\delta}_2} \\ & + T_3(V_\pi, V_\sigma, \theta) e^{i\mathbf{k}\cdot\boldsymbol{\delta}_3}, \end{aligned} \tag{C3}$$

where

$$\begin{aligned} \boldsymbol{\delta}_1 &= (-\cos\theta\sqrt{3}/2, \cos\theta/2, \sin\theta) a/\sqrt{3}, \\ \boldsymbol{\delta}_2 &= (\cos\theta\sqrt{3}/2, \cos\theta/2, \sin\theta) a/\sqrt{3}, \\ \boldsymbol{\delta}_3 &= (0, -\cos\theta, \sin\theta) a/\sqrt{3} \end{aligned} \tag{C4}$$

in terms of the lattice constant a as shown in Fig. 8. The side of the hexagon is $a/\sqrt{3}$. Here T_1, T_2, T_3 can be expressed in terms of the V_π and V_σ components of the nearestins-neighbor hopping interaction using the Koster-Slater two-center approximation [49]. We assume here that under buckling, the bond distance a is kept fixed and the buckling angle just changes the relative contributions of V_π and V_σ to the hopping integrals. We chose the V_π/V_σ ratio to be -0.275. This value is close to Walter Harrison's universal ratio [50]. Together with the $\Delta_{x,y} - \Delta_\sigma$ parameters, they were chosen to present a similar band structure to the DFT results of the main paper. However, a detailed fit was not attempted because the actual band structure is affected by interaction with nearby d and s bands and the main purpose of our tight-binding model is to study the generic behavior of the bands as function of buckling angle and mostly the topological features.

TABLE VI. Character table for D_{3d}.

D_{3d}		E	$2C_3$	$3U'_2$	i	$2S_6$	$3\sigma'_v$
Γ_1^+	A_{1g}	1	1	1	1	1	1
Γ_2^+	A_{2g}	1	1	-1	1	1	-1
Γ_3^+	E_g	2	-1	0	2	-1	0
Γ_1^-	A_{1u}	1	1	1	-1	-1 -1	
Γ_2^-	A_{2u}	1	1	-1	-1	-1	1
Γ_3^-	E_u	2	-1	0	-2	1	0

TABLE VII. Compatibility between D_{6h} and D_{3d} group irreps.

D_{6h}	A_{1g}	A_{2g}	B_{1g}	B_{2g}	E_{2g}	E_{1g}
D_{3d}	A_{1g}	A_{2g}	A_{2g}	A_{1g}	E_g	E_g

Each T_i is a 3×3 matrix in the basis of the p_m, $m = (x, y, z)$ orbitals.

$$T_1(V_\pi, V_\sigma, \theta) = \begin{bmatrix} V_\pi\left(-\frac{3\cos^2\theta}{4}+1\right)+V_\sigma\frac{3\cos^2\theta}{4} & (V_\pi - V_\sigma)\frac{\sqrt{3}\cos^2\theta}{4} & (V_\pi - V_\sigma)\frac{\sqrt{3}\sin\theta\cos\theta}{2} \\ (V_\pi - V_\sigma)\frac{\sqrt{3}\cos^2\theta}{4} & V_\pi\left(-\frac{\cos^2\theta}{4}+1\right)+V_\sigma\frac{\cos^2\theta}{4} & (V_\sigma - V_\pi)\frac{\sin\theta\cos\theta}{2} \\ (V_\pi - V_\sigma)\frac{\sqrt{3}\sin\theta\cos\theta}{2} & (V_\sigma - V_\pi)\frac{\sin\theta\cos\theta}{2} & V_\pi\cos^2\theta + V_\sigma\sin^2\theta \end{bmatrix}, \tag{C5}$$

$$T_2(V_\pi, V_\sigma, \theta) = \begin{bmatrix} V_\pi\left(-\frac{3\cos^2\theta}{4}+1\right)+V_\sigma\frac{3\cos^2\theta}{4} & (V_\sigma - V_\pi)\frac{\sqrt{3}\cos^2\theta}{4} & (V_\sigma - V_\pi)\frac{\sqrt{3}\sin\theta\cos\theta}{2} \\ (V_\sigma - V_\pi)\frac{\sqrt{3}\cos^2\theta}{4} & V_\pi\left(-\frac{\cos^2\theta}{4}+1\right)+V_\sigma\frac{\cos^2\theta}{4} & (V_\sigma - V_\pi)\frac{\sin\theta\cos\theta}{2} \\ (V_\sigma - V_\pi)\frac{\sqrt{3}\sin\theta\cos\theta}{2} & (V_\sigma - V_\pi)\frac{\sin\theta\cos\theta}{2} & V_\pi\cos^2\theta + V_\sigma\sin^2\theta \end{bmatrix}, \tag{C6}$$

$$T_3(V_\pi, V_\sigma, \theta) = \begin{bmatrix} V_\pi & 0 & 0 \\ 0 & V_\pi\sin^2\theta + V_\sigma\cos^2\theta & (V_\pi - V_\sigma)\sin\theta\cos\theta \\ 0 & (V_\pi - V_\sigma)\sin\theta\cos\theta & V_\pi\cos^2\theta + V_\sigma\sin^2\theta \end{bmatrix}. \tag{C7}$$

It is insightful to first understand the unbuckled case ($\theta = 0$). In that case, the p_z orbitals are decoupled from the p_x, p_y orbitals because the former are odd with respect to the horizontal mirror plane and the latter are even.

The z part of the Hamiltonian becomes the well-known

$$H_z(\mathbf{k}) = \begin{bmatrix} \Delta_z & V_\pi g_0(\mathbf{k}) \\ V_\pi g_0^*(\mathbf{k}) & \Delta_z \end{bmatrix} \tag{C8}$$

with

$$g_0(\mathbf{k}) = \sum_{j=1}^{3} e^{i\mathbf{k}\cdot\boldsymbol{\delta}_j} \tag{C9}$$

giving the purely π-bonded bands. At Γ we find $E(\mathbf{k}_\Gamma) = \Delta_z \pm 3V_\pi$ with eigenvectors $\frac{p_{zA}\mp p_{zB}}{\sqrt{2}}$. At K, we have $e^{i\mathbf{k}\cdot\boldsymbol{\delta}_1} = e^{-i2\pi/3}$, $e^{i\mathbf{k}\cdot\boldsymbol{\delta}_2} = e^{i2\pi/3}$ $e^{i\mathbf{k}\cdot\boldsymbol{\delta}_1} = 1$ and $g_0(\mathbf{k}) = 0$ giving the doubly degenerate eigenvalue Δ_z. This is the Dirac point E''.

The xy part of the Hamiltonian has the off-diagonal part

$$\bar{H}_{xy} = \begin{bmatrix} \frac{3V_\sigma+V_\pi}{4}g_+(\mathbf{k}) + V_\pi e^{i\mathbf{k}\cdot\boldsymbol{\delta}_3} & \frac{\sqrt{3}(V_\pi - V_\sigma)}{4}g_-(\mathbf{k}) \\ \frac{\sqrt{3}(V_\pi - V_\sigma)}{4}g_-(\mathbf{k}) & \frac{3V_\pi+V_\sigma}{4}g_+(\mathbf{k}) + V_\sigma e^{i\mathbf{k}\cdot\boldsymbol{\delta}_3} \end{bmatrix} \tag{C10}$$

with $g_\pm(\mathbf{k}) = e^{i\mathbf{k}\cdot\boldsymbol{\delta}_1} \pm e^{i\mathbf{k}\cdot\boldsymbol{\delta}_2}$. At Γ, the $g_-(\mathbf{k}_\Gamma) = 0$ and we obtain two degenerate eigenvalues $\Delta_{x,y} \pm (V_\sigma + V_\pi)3/2$ with eigenstates $(p_{xA} \mp p_{xB})/\sqrt{2}$ and $(p_{yA} \mp p_{yB})/\sqrt{2}$. At K, the matrix can still be diagonalized analytically. The off-diagonal part here takes the form

$$\bar{H}_{xy}(\mathbf{k}_K) = \begin{bmatrix} -\frac{3}{4}(V_\sigma - V_\pi) & i\frac{3}{4}(V_\sigma - V_\pi) \\ i\frac{3}{4}(V_\sigma - V_\pi) & \frac{3}{4}(V_\sigma - V_\pi) \end{bmatrix} \tag{C11}$$

TABLE VIII. Character table of C_{2h}.

C_{2h}		E	$U'_{2(x)}$	i	$\sigma'_{v(yz)}$
M_1^+	A_g	1	1	1	1
M_2^+	B_g	1	−1	1	−1
M_1^-	A_u	1	1	−1	−1
M_2^-	B_u	1	−1	−1	1

The Hamiltonian then has a double degenerate eigenvalue $E = \Delta_\pi$ with eigenvectors $\pi_A = (p_{xA} + ip_{yA})/\sqrt{2}$ and $\pi_B^* = (p_{xB} - ip_{yB})/\sqrt{2}$, the Dirac point E', and two nondegenerate eigenvalues $\Delta_{x,y} + (V_\pi - 3V_\sigma)/2$ with eigenvector $(\pi_A^* - \pi_B)/\sqrt{2}$ $\Delta_{x,y} - (V_\pi - 3V_\sigma)/2)$ with eigenvector $(\pi_A^* + \pi_B)/\sqrt{2}$. In other words, it can be diagonalized in the basis of the π_A, π_A^*, π_B and π_B^* orbitals [30].

We now examine the band surfaces in 3D, in particular the intersection of the down pointing Dirac cone derived from the p_x, p_y orbitals and the upward pointing Dirac cone derived from the p_z orbitals. To further study this crossing analytically we expand the tight-binding Hamiltonian around K, i.e., for $\mathbf{k} = \mathbf{k}_K + \mathbf{q}$ for small $\mathbf{q} = (q\cos\phi, q\sin\phi)$. The azimuthal angle ϕ of the $\mathbf{q}$ is measured from the X direction for the K point along x and $q = |\mathbf{q}|$.

The eigenvalues are symmetric about the Δ_z and $\Delta_{x,y}$ and given by

$$\begin{aligned} E_z &= \Delta_z \pm v_z q \pm \frac{q^2}{m_z}\cos(3\phi), \\ E_{x,y} &= \Delta_{x,y} \pm v_{x,y} q \pm \frac{q^2}{m_{x,y}}\cos(3\phi). \end{aligned} \tag{C12}$$

Here, v_z and $v_{x,y}$ are the Dirac linear dispersion velocities and m_z and $m_{x,y}$ are an effective mass parameter. The actual effective masses depend on the direction of $\mathbf{q}$ leading to a warping of the constant energy lines with threefold symmetry, while the velocity is isotropic. For the p_z Hamiltonian, one finds in our nearest-neighbor tight-binding Hamiltonian, $v_z = \sqrt{3}\pi V_\pi$ and $m_z^{-1} = -V_\pi\pi^2/2$. Thus both are completely determined by the V_π-interaction between p_z orbitals. On the other hand, one may also keep m_z and v_z as independent parameters to make the effective low-energy Hamiltonian and eigenvalues applicable beyond the tight-binding model. Their form is dictated by symmetry.

TABLE IX. Character table of C_2.

C_2		E	$U'_{2(x)}$
T_1	A	1	1
T_2	B	1	−1

TABLE X. Character table of C_s.

C_s		E	$\sigma'_{v(yz)}$
Σ_1	A'	1	1
Σ_2	A''	1	-1

For the $\{p_x, p_y\}$ derived bands, the eigenvalues of the tight-binding Hamiltonian are also found to be symmetric about Δ_π and are found by diagonalizing $H_{\text{eff}} = \bar{H}_{xy}\bar{H}_{xy}^{\dagger}$ and taking $\pm\sqrt{\lambda}$ of its eigenvalues λ. These eigenvalues were worked out by Wu *et al.* [30] for the special case that $V_\pi = 0$, which applies to optical lattices. In that case, two bands are found to be flat, and two are Dirac cone like and have exactly the same shape as for the p_z orbitals. With a mixture of both V_σ and V_π, the expressions of the expansion in q become too complex to be useful but the important finding is that by choosing the $m_{x,y}$ of opposite sign as the m_z orbitals the warping is found to be rotated by 30°. In the DFT band structure in the main paper we can see that the particle-hole symmetry about $\Delta_{x,y}$ which is the E' value above the Fermi level, no longer holds. This is because of the interactions with the higher lying bands which are derived from the Sb-d orbitals and not included in the model. Therefore it is not that useful to find expressions for the velocity and mass parameter of this Dirac cone in terms of the tight-binding model because the latter has only limited validity. What matters is that both Dirac cone bands near K and extending up to the region of their intersection can be described by Eq. (C12), which represents two trigonally warped Dirac cones and that in the DFT results these cones are found to be rotated 30° with respect to each other.

Examining the bands in Fig. 1 in the main paper one can see that the upper band of the p_z derived Dirac cone deviates upward from the linear behavior and thus has positive m_z which agrees with the $V_\pi < 0$. The lower band of the $p_{x,y}$ derived Dirac cone can be seen to bend down and thus has the opposite mass $m_{x,y} < 0$. Note that the direction K-Γ corresponds to $\phi = \pi$. and the direction $K - M$ corresponds to $\phi = 2\pi/3$.

Both of the Dirac cones can be obtained from an effective low Hamiltonian of the form

$$H_{\text{eff}} = \begin{bmatrix} \Delta_z & qv_z + q^2\frac{\cos(3\phi)}{m_z} \\ qv_z + q^2\frac{\cos(3\phi)}{m_z} & \Delta_z \end{bmatrix} \tag{C13}$$

with a similar one for the $p_{x,y}$ case.

To illustrate the behavior of the Dirac cone warping, we show in Fig. 9 contour plots obtained in the tight-binding Hamiltonian for different choices of V_σ, V_π for the p_z derived and $\{p_x, p_y\}$ derived cones. One can see that while for the

TABLE XI. Character table of C_3, $\omega = e^{2i\pi/3}$.

C_3		E	C_3	C_3^{-1}
K_1	A	1	1	1
K_2	E	1	ω	ω^*
K_3	E	1	ω^*	ω

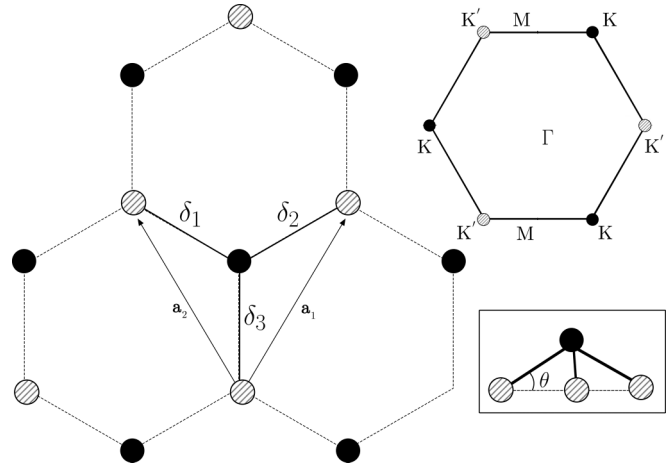

FIG. 8. Lattice of low buckled antimonene. Shaded and dark circles represent the Sb at different height. Inset shows the definition of buckling used in the paper along with the corresponding 1^{st} *BZ*.

p_z derived ones the corners of the triangular contours around K are point in the K-M-K' direction and the shape does not depend on V_σ because these bands only involve V_π. In contrast the $\{p_x, p_y\}$ derived cones for the first choice of V_σ, V_π parameters which best matches the DFT bands and are used in the main paper, the cones are rotated by 30° with respect to the p_z cone. The flat edge of the triangle is now along the K-M-K' direction. However, as we change the V_σ, V_π these cones can become almost circular (middle case) or their warping rotated the same as for p_z as V_σ is increased. Thus the rotated warping of the p_z relative to the $\{p_x, p_y\}$ derived cones is sensitive to the relative values of V_σ and V_π and this is what is ultimately responsible for the shape of the nodal line and the occurrence of six Dirac points after buckling.

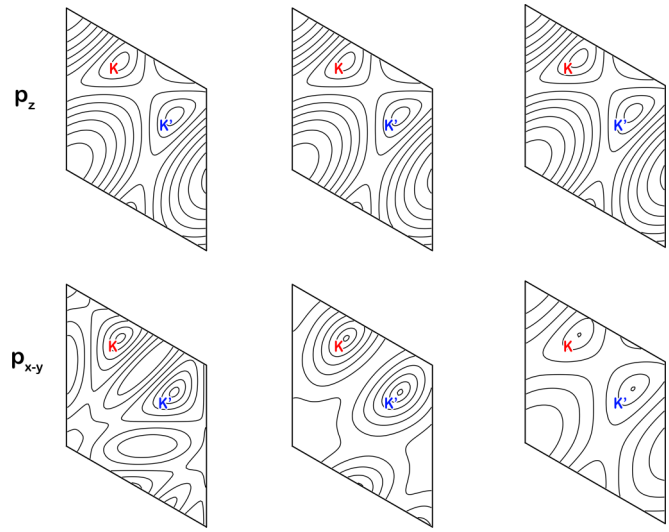

FIG. 9. Contour plot of valence p_z (top) and conduction $\{p_x, p_y\}$ (bottom) bands for various values of (V_π, V_σ). From left to right, $(V_\pi, V_\sigma) = (-0.66, 2.4), (-0.66, 3.6), (-0.66, 4.44)$ eV. K and K' points are marked. The Γ point occurs at each of the corners of the reciprocal unit cell spanned by $\mathbf{b}_1$ and $\mathbf{b}_2$.

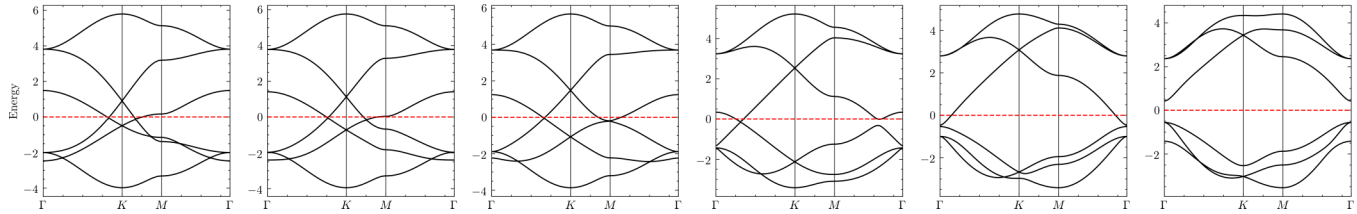

FIG. 10. Evolution of band structure(in eV) at different buckling angles θ. From left to right) 0°, 5°, 7.34°, 20°, 36°. In this figure, the energy units are eV and $V_\sigma = 2.4$ eV and $V_\pi = -0.66$ eV. The red-dashed line at 0 energy is the Fermi energy in the flat case but is kept fixed in the later figures without adjusting the Fermi energy. In the before last panel, the Fermi energy lies exactly at the degenerate band touching at Γ.

The effects of buckling in our model are incorporated through the θ dependence. As already explained in the main text, when $\theta \neq 0$ the off-diagonal terms between the p_z block and $\{p_x, p_y\}$ blocks are turned on. The resulting 6×6 matrix is readily diagonalized numerically but analytic expressions are no longer possible. Instead in the main text we then focus on the effective low energy Hamiltonian near the nodal line, which explains its breaking up into six separate Dirac points.

In Fig. 10, we show the tight-binding bands of the 6×6 p-orbital derived Hamiltonian for various buckling angles. The leftmost figure for the flat case can be compared with the DFT results given in Fig. 1(a) of the main paper. The V_σ, V_π and $\Delta_{x,y}$, Δ_z parameters were chosen to give about the correct ratios of the splitting of the two Dirac points E', E'' at K, the splitting of the outermost eigenvalues A_2', A_1' [see labeling of Fig. 1(a) in main paper] of the $\{p_x, p_y\}$ derived bands at K and the splitting of the p_z derived bands at Γ. Note that both the $\{p_x, p_y\}$ derived bands and p_z derived bands are 'particle-hole' symmetric about their center of gravity, the E' and E'' Dirac points at K, which are displaced from each other by $\Delta_{x,y} - \Delta_z$ for the flat case. We can see that the lower band levels A_{2u}, E_{2g} at Γ are then close to each other while the upper band levels at Γ, B_{2g} and E_{1u} are more separated and inverted from the DFT bands. We are not trying to reproduce the DFT bands exactly because these upper bands are influenced by the interaction with the Sb-d bands in the DFT results. Our main goal here is just to see the qualitative evolution of the bands under buckling. We can see the Dirac points move toward M, disappear at M and then the remaining ones move closer to Γ and finally the full gap opens.

APPENDIX D: WINDING NUMBER

One can calculate the winding number of the Dirac cones around a contour C around the Dirac point given by [33]

$$W_c = \frac{1}{2\pi} \oint_C \nabla_q \phi_{\vec{q}} \cdot dq \tag{D1}$$

where $\phi_{\vec{q}}$ is the relative phase between the two coefficients in the eigenvector $\tan(\phi_{\vec{q}}) = \frac{u_2}{u_1}$ of the 2×2 effective Hamiltonian near the Dirac point [Eq. (4) in the main paper]. Alternatively, in the tight-binding model, we can open up a gap at each of these Dirac cones by adding the μ_A, μ_B parameters giving a different on-site energy to the A and B atoms in the unit cell. Once a small gap is opened up, the Berry curvature [51,52], i.e., the curl of the Berry connection, is calculated numerically on a fine $\mathbf{k}$ mesh and for each occupied state. Summing these gives the total winding number as shown in Fig. 3(b) in the main part of the paper. Finally, also in the tight-binding model, we can calculate the accumulated Berry phase along a small contour around the Dirac point. We have verified that these different procedures agree with each other.

APPENDIX E: RESULTS FOR ARSENENE

While the main paper is mostly focused on antimonene (Sb), very similar results hold for arsenene (As). The relative stability of the flat and buckled honeycomb structure was already shown in Fig. 6. The band structure at the GGA level is shown in Fig. 11 both with and without spin-orbit coupling. We can see that the Fermi level again occurs near the crossing of the two Dirac cones centered at K. The crossings of these cones along Γ-K and K-M are again tilted with respect to each other. The spin-orbit coupling opens a gap at all the Dirac points. We can see that as in Sb, the spin-orbit opened gap is larger for the upper E' $\{p_x, p_y\}$ derived Dirac point at K than for the lower E'' p_z derived Dirac point. At the new Dirac points along Γ-K and K-M, the splitting is intermediate. The main point is that the gaps opened here at the Dirac points near E_F are straddled with respect to each other so that the system remains overall metallic, in contrast with the Sb case in the main paper Fig. 3, where a zero indirect gap situation emerges.

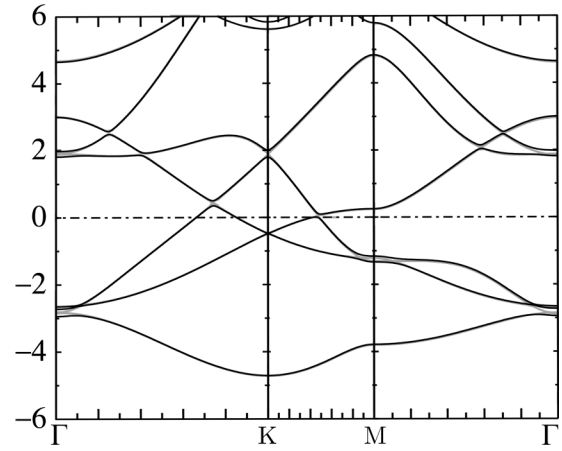

FIG. 11. Band structure of arsenene (As) with (black) and without (red) SOC at the GGA level.

[1] K. S. Novoselov, A. K. Geim, S. V. Morozov, D. Jiang, Y. Zhang, S. V. Dubonos, I. V. Grigorieva, and A. A. Firsov, Science **306**, 666 (2004).

[2] P. Ares, J. J. Palacios, G. Abellán, J. Gómez-Herrero, and F. Zamora, Adv. Mater. **30**, 1703771 (2018).

[3] H.-S. Tsai, S.-W. Wang, C.-H. Hsiao, C.-W. Chen, H. Ouyang, Y.-L. Chueh, H.-C. Kuo, and J.-H. Liang, Chem. Mater. **28**, 425 (2016).

[4] J. Ji, X. Song, J. Liu, Z. Yan, C. Huo, S. Zhang, M. Su, L. Liao, W. Wang, Z. Ni, Y. Hao, and H. Zeng, Nat. Commun. **7**, 13352 (2016), article.

[5] O. U. Aktürk, V. O. Özçelik, and S. Ciraci, Phys. Rev. B **91**, 235446 (2015).

[6] G. Wang, R. Pandey, and S. P. Karna, ACS Appl. Mater. Interfaces **7**, 11490 (2015).

[7] S. Zhang, Z. Yan, Y. Li, Z. Chen, and H. Zeng, Angew. Chem., Int. Ed. **54**, 3112 (2015).

[8] C. Kamal and M. Ezawa, Phys. Rev. B **91**, 085423 (2015).

[9] L. Li, Y. Yu, G. J. Ye, Q. Ge, X. Ou, H. Wu, D. Feng, X. H. Chen, and Y. Zhang, Nat. Nanotechnol. **9**, 372 (2014).

[10] J. Sone, T. Yamagami, Y. Aoki, K. Nakatsuji, and H. Hirayama, New J. Phys. **16**, 095004 (2014).

[11] M. E. Dávila and G. Le Lay, Sci. Rep. **6**, 20714 (2016).

[12] Y. Shao, Z.-L. Liu, C. Cheng, X. Wu, H. Liu, C. Liu, J.-O. Wang, S.-Y. Zhu, Y.-Q. Wang, D.-X. Shi, K. Ibrahim, J.-T. Sun, Y.-L. Wang, and H.-J. Gao, Nano Lett. **18**, 2133 (2018).

[13] F.-C. Chuang, C.-H. Hsu, C.-Y. Chen, Z.-Q. Huang, V. Ozolins, H. Lin, and A. Bansil, Appl. Phys. Lett. **102**, 022424 (2013).

[14] H. Lu, J. Gao, Z. Hu, and X. Shao, RSC Adv. **6**, 102724 (2016).

[15] Z.-Q. Huang, C.-H. Hsu, F.-C. Chuang, Y.-T. Liu, H. Lin, W.-S. Su, V. Ozolins, and A. Bansil, New J. Phys. **16**, 105018 (2014).

[16] G. Bian, X. Wang, Y. Liu, T. Miller, and T.-C. Chiang, Phys. Rev. Lett. **108**, 176401 (2012).

[17] P. F. Zhang, Z. Liu, W. Duan, F. Liu, and J. Wu, Phys. Rev. B **85**, 201410(R) (2012).

[18] M. Zhao, X. Zhang, and L. Li, Sci. Rep. **5**, 16108 (2015).

[19] C.-H. Hsu, Z.-Q. Huang, C. P. Crisostomo, L.-Z. Yao, F.-C. Chuang, Y.-T. Liu, B. Wang, C.-H. Hsu, C.-C. Lee, H. Lin, and A. Bansil, Sci. Rep. **6**, 18993 (2016).

[20] F. Schindler, M. Brzezińska, W. A. Benalcazar, M. Iraola, A. Bouhon, S. S. Tsirkin, M. G. Vergniory, and T. Neupert, Phys. Rev. Res. **1**, 033074 (2019).

[21] J. P. Perdew, K. Burke, and M. Ernzerhof, Phys. Rev. Lett. **77**, 3865 (1996).

[22] M. van Schilfgaarde, T. Kotani, and S. Faleev, Phys. Rev. Lett. **96**, 226402 (2006).

[23] T. Kotani, M. van Schilfgaarde, and S. V. Faleev, Phys. Rev. B **76**, 165106 (2007).

[24] L. Hedin, Phys. Rev. **139**, A796 (1965).

[25] L. Hedin and S. Lundqvist, in *Solid State Physics, Advanced in Research and Applications*, edited by F. Seitz, D. Turnbull, and H. Ehrenreich (Academic, New York, 1969), Vol. 23, pp. 1–181.

[26] M. Methfessel, M. van Schilfgaarde, and R. A. Casali, in *Electronic Structure and Physical Properties of Solids. The Use of the LMTO Method*, edited by H. Dreyssé, Lecture Notes in Physics Vol. 535 (Springer Verlag, Berlin, 2000), p. 114.

[27] T. Kotani and M. van Schilfgaarde, Phys. Rev. B **81**, 125117 (2010).

[28] D. Pashov, S. Acharya, W. R. Lambrecht, J. Jackson, K. D. Belashchenko, A. Chantis, F. Jamet, and M. van Schilfgaarde, Comput. Phys. Commun. **249**, 107065 (2020).

[29] The questaal code package is available at http://www.questaal.org.

[30] C. Wu and S. Das Sarma, Phys. Rev. B **77**, 235107 (2008).

[31] B. He, Y. Wang, M. Q. Arguilla, N. D. Cultrara, M. R. Scudder, J. E. Goldberger, W. Windl, and J. P. Heremans, Nat. Mater. **18**, 568 (2019).

[32] S. Ahn, E. J. Mele, and H. Min, Phys. Rev. Lett. **119**, 147402 (2017).

[33] M. Goerbig and G. Montambaux, in *Progress in Mathematical Physics*, edited by B. Duplantier, V. Rivasseau, and J.-N. Fuchs (Springer International Publishing, Cham, Switzerland, 2017), Vol. 71, pp. 25–53.

[34] G. Montambaux, F. Piéchon, J.-N. Fuchs, and M. O. Goerbig, Phys. Rev. B **80**, 153412 (2009).

[35] Y. Hasegawa, R. Konno, H. Nakano, and M. Kohmoto, Phys. Rev. B **74**, 033413 (2006).

[36] P. Dietl, F. Piéchon, and G. Montambaux, Phys. Rev. Lett. **100**, 236405 (2008).

[37] S. K. Radha and W. R. L. Lambrecht, arXiv:2003.12656.

[38] S. Zhang, W. Zhou, Y. Ma, J. Ji, B. Cai, S. A. Yang, Z. Zhu, Z. Chen, and H. Zeng, Nano Lett. **17**, 3434 (2017).

[39] M. Gonçalves, P. Ribeiro, R. Mondaini, and E. V. Castro, Phys. Rev. Lett. **122**, 126601 (2019).

[40] S. Ryu and Y. Hatsugai, Phys. Rev. Lett. **89**, 077002 (2002).

[41] P. Giannozzi, S. Baroni, N. Bonini, M. Calandra, R. Car, C. Cavazzoni, D. Ceresoli, G. L. Chiarotti, M. Cococcioni, I. Dabo, A. D. Corso, S. de Gironcoli, S. Fabris, G. Fratesi, R. Gebauer, U. Gerstmann, C. Gougoussis, A. Kokalj, M. Lazzeri, L. Martin-Samos, N. Marzari, F. Mauri, R. Mazzarello, S. Paolini, A. Pasquarello, L. Paulatto, C. Sbraccia, S. Scandolo, G. Sclauzero, A. P. Seitsonen, A. Smogunov, P. Umari, and R. M. Wentzcovitch, J. Phys.: Condens. Matter **21**, 395502 (2009).

[42] R. Bianco, I. Errea, L. Paulatto, M. Calandra, and F. Mauri, Phys. Rev. B **96**, 014111 (2017).

[43] X. Gong, Z. Hu, Y. Huang, and X. Shao, J. Alloys Compd. **767**, 552 (2018).

[44] Y.-p. Wang, W.-x. Ji, C.-w. Zhang, P. Li, F. Li, M.-j. Ren, X.-L. Chen, M. Yuan, and P.-j. Wang, Sci. Rep. **6**, 20342 (2016).

[45] E. Kogan and V. U. Nazarov, Phys. Rev. B **85**, 115418 (2012).

[46] E. Kogan, V. U. Nazarov, V. M. Silkin, and M. Kaveh, Phys. Rev. B **89**, 165430 (2014).

[47] S. Minami, I. Sugita, R. Tomita, H. Oshima, and M. Saito, Jpn. J. Appl. Phys. **56**, 105102 (2017).

[48] G. F. Koster, J. O. Dimmock, R. G. Wheeler, and H. Statz, *Properties of the Thierty-Two Point Groups* (MIT Press, Cambridge, MA, 1963).

[49] J. C. Slater and G. F. Koster, Phys. Rev. **94**, 1498 (1954).

[50] S. Froyen and W. A. Harrison, Phys. Rev. B **20**, 2420 (1979).

[51] D. Gresch, G. Autès, O. V. Yazyev, M. Troyer, D. Vanderbilt, B. A. Bernevig, and A. A. Soluyanov, Phys. Rev. B **95**, 075146 (2017).

[52] D. Vanderbilt, *Berry Phases in Electronic Structure Theory: Electric Polarization, Orbital Magnetization and Topological Insulators* (Cambridge University Press, Cambridge, 2018).